


Electrowetting of a leaky dielectric droplet under a time-periodic electric field

Dipin S. Pillai ^{*}

Department of Chemical Engineering, Indian Institute of Technology Kanpur, Uttar Pradesh 208016, India

Kirti Chandra Sahu 

*Department of Chemical Engineering, Indian Institute of Technology Hyderabad,
Sangareddy, Telangana, 502 285, India*

Ranga Narayanan 

Department of Chemical Engineering, University of Florida, Gainesville, Florida 32611, USA



(Received 27 August 2020; accepted 1 June 2021; published 2 July 2021)

The wetting and contact line dynamics of a leaky dielectric sessile droplet under an alternating (ac) electrostatic field applied in the vertical direction is investigated. A thin precursor film-based reduced-order model using the weighted residual integral boundary layer technique is developed. The limiting cases of perfect conducting and perfect dielectric droplets are also considered. It is shown that the droplet oscillates with a frequency twice that of the forcing potential due to the quadratic dependence of the Maxwell stress on the applied ac electric field. These oscillations take place about an equilibrium configuration, which can be achieved with a constant (dc) electric potential equivalent to the root-mean-square potential of the applied ac field. It is also shown that the contact line motion increases monotonically with the amplitude of the ac electric forcing. A significant increase in ac field leads to spiking and the interface ruptures at the top electrode. Depending on the static contact angle, the droplet deformation can become nonmonotonic as the applied frequency of the ac electric field increases. This behavior is attributed to the competition between the timescale of forcing and the timescale of the response as affected by the drop's wettability. The role of conductivity ratio, permittivity ratio, and different waveforms of ac forcing are also investigated.

DOI: [10.1103/PhysRevFluids.6.073701](https://doi.org/10.1103/PhysRevFluids.6.073701)

I. INTRODUCTION

Microfluidic systems can be broadly classified into two types: the flow-based “continuous” and the discrete droplet-based “digital” lab-on-chip devices [1]. While the former handles continuous throughput of the working fluids, the latter is based on manipulating discrete fluid droplets. Due to the characteristic low length scales and the associated low Reynolds numbers in microfluidic devices, achieving good mixing becomes difficult. Although continuous microfluidic devices typically employ chaotic advection as a means to achieving good mixing [2], their realization inevitably consumes large real estate on the chip. Digital microfluidics with droplet actuation, thus provide an alternative means toward achieving mixing on the spot [3]. In addition, spreading and actuation of sessile droplets find great technological relevance in diverse applications ranging from medical diagnostics to microelectronics [4]. A detailed review of the physics of wetting dynamics of a sessile droplet can be found in de Gennes [5], Teletzke *et al.* [6], Bonn *et al.* [7], and Brutin [8].

^{*}dipinsp@iitk.ac.in

There are several ways one can achieve droplet actuation on solid substrates, such as piezoelectrically induced mechanical transduction [9] or thermocapillarity driven actuation by imposing temperature gradients along the substrate or at the droplet interface [10,11]. Electrowetting provides a convenient method to tune the wettability characteristics of the substrate and thereby induce droplet actuation using an externally applied electric field [12]. There are two electrode configurations typically employed in electrowetting-induced actuation of droplets [13], namely the open “needle-electrode” and the closed “coplanar” configurations. In the open needle-electrode configuration, a needle immersed inside the droplet acts as one of the electrodes, while the substrate acts as the other electrode. On the other hand, in the closed coplanar configuration, the droplet sits on an electrode but does not come in direct contact with the top electrode. In the needle-electrode configuration, the droplet is usually a good conductor, while the substrate is a perfect dielectric. This configuration is therefore also known as electro-wetting on dielectric (EWOD). A sessile droplet in EWOD exhibits a large equilibrium contact angle due to a layer of coating. At low magnitudes of the applied electric field, the static contact angle decreases with an increase in the electric field, following the well-known Young-Lippmann equation. The contact angle, however, saturates at higher voltages, which is a phenomenon not well understood and is an area of active research [14]. Application of periodic ac fields is particularly significant as it avoids electrophoresis, which is observed under constant dc forcing. Moreover, the contact-angle saturation observed at high dc voltages is known to be delayed by employing an ac field [15]. Further, by solely tuning the frequency of the ac field, one can manipulate the droplet response for fluids that exhibit characteristics that range from a leaky dielectric to a perfect dielectric. A general mathematical formulation for the electrohydrodynamic description of low-conducting fluids was given by Saville [16] and since then has been known as the leaky dielectric theory. It is based on the assumption that the typical timescale associated with charge relaxation is much smaller than the hydrodynamic timescale. Therefore, the charges are confined to the interface separating the fluids and the charges in the fluid bulk can be assumed to be zero. On the other hand, in the case of a perfect dielectric medium, the timescale associated with the generation of free charges is much larger than the viscous timescale. Thus it can be assumed that there are no free charges in the entire domain.

A sessile droplet has been shown to spread spontaneously under a dc electric field due to electrostatic reduction of the interfacial energy between droplet and substrate [4]. The computed static deformed shapes under such fields have been limited by either constant contact angles or by the assumption of pinned contact lines [17,18]. Computational studies on the transient dynamics of a sessile droplet under the application of dc field predict the contact line motion as well as the effect of inertia leading to the formation of microjets from the droplet tip for high electrical fields [19,20]. Experimental studies by Bateni *et al.* [21] have demonstrated that sessile droplets of polar fluids exhibit an increase in contact angle under steady electric fields, regardless of the field polarity. However, for nonpolar sessile droplets, such an influence of the electric field was not found.

Studies on oscillating sessile droplets have yielded interesting results with either the application of pure dc fields or ac fields. In particular, Mugele *et al.* [3] showed experimentally that mixing in sessile droplets can be achieved by self-induced oscillations caused by electrowetting. The oscillations were found to result from the droplet undergoing attachment-detachment cycles with respect to a needle-electrode immersed in it. They concluded that mixing obtained in this process was nonchaotic as their experiments did not exhibit any logarithmic scaling of mixing time with the Péclet number, a characteristic of chaotic mixing. However, in subsequent studies, they showed that the droplet oscillations induced by an ac electric forcing can result in chaotic mixing instead of the attachment-detachment cycles seen earlier [22]. It has been showed that ac electrowetting can be employed as a means to induce stirring flows in sessile droplets for biochemical reaction enhancement and handling of cells [23]. Several numerical investigations on ac electrowetting and contact line dynamics have shown agreement with experiments and in some cases, demonstrated the importance of Joule heating at very high forcing frequencies [24,25]. In recent work, relevant to the current study, Sahu *et al.* [26] have shown that for leaky dielectric fluids, the mean amplitude

of shape oscillations of a droplet subjected to an alternating electric field may deviate from the steady-state deformation under an equivalent root-mean-squared (RMS) direct electric field.

It is clear from the above that there have been several studies on electrohydrodynamics of a sessile droplet under the influence of a dc electric field, with far less attention being given to the case of ac electric fields, a subject of considerable practical and scientific interest. In the current work, an inertial lubrication model based on the weighted residual integral boundary layer (WRIBL) method [27] is developed to study the behavior of a sessile droplet under a time-periodic electrostatic forcing. We consider a closed coplanar configuration of the sessile droplet. The droplet and the ambient hydrodynamically passive medium are taken to be leaky dielectric [16]. Following the work of Gomba and Homsy [10], we use a one-dimensional (1D) description of the sessile droplet based on thin precursor film model to capture the droplet dynamics. It was shown by them that a sessile droplet subject to thermocapillary forces is described well using such a model. The droplet contact line as well as its interfacial dynamics are investigated over various parameter regimes. The two limiting cases, namely, the perfect conducting droplet and the perfect dielectric droplet have also been investigated and the dynamics is compared with that of the leaky dielectric drop.

We investigate the shape dynamics of a sessile leaky dielectric drop in the presence of an alternating electric field. The presence of ac field results in an enhanced contact line motion and droplet shape deformation under favorable forcing frequencies. Its implications have applications in obtaining optimal mixing conditions in droplet microfluidics. In the current work, we show that the contact line oscillates in the presence of an ac field with a frequency twice that of the forcing potential due to the quadratic dependence of the Maxwell stress on the applied electric field. The study on the influence of varying frequency of the applied ac electric field reveals that the amplitude of the response oscillations is almost constant at low frequencies, which increases in the intermediate range of frequencies, followed by a steep decrease with further increase in frequency of the ac field. At high frequencies, as the timescale associated with electric potential change is much smaller than the capillary timescale of the droplet, the contact line remains almost static as if the droplet is under the influence of an equivalent dc field in the RMS sense. We also investigate different waveforms of the applied ac electric field on the dynamics of the sessile droplet and find that a square waveform effectively acts like a static dc electric field.

The paper is organized as follows. In Sec. II, the problem is formulated and the WRIBL model governing the electrowetting dynamics of a sessile droplet is derived. The results of interface evolution and the underlying physics are discussed in Sec. III with concluding remarks given in Sec. IV.

II. MATHEMATICAL MODEL

The electrohydrodynamics of a sessile droplet (*fluid 1*) placed on an electrically conducting substrate under the influence of an ac electric field is studied, as shown in the schematic diagram [Fig. 1(a)]. A Cartesian coordinate system with the origin at the bottom electrode along the droplet center-line is used, as depicted in the Fig. 1(a). This choice of coordinate system is employed based on its success in predicting the underlying physics of sessile droplet dynamics in several earlier studies; see, for instance, the work on thermocapillary actuation of droplets [10]. While we lose out on accurate quantitative predictions, this simplified geometry helps us to glean significant insight into the physics of the problem. Three types of ac electric field waveforms are considered as shown in Fig. 1(b). Following earlier works [10], a thin precursor film has been introduced on the horizontal substrate. The presence of the precursor film ensures that any singularity associated with the triple contact line dynamics and Maxwell stress does not arise. The fluids are assumed to be Newtonian and leaky dielectric. However, in order to contrast the droplet dynamics obtained for the leaky dielectric medium, the limiting cases of the perfect conducting and the perfect dielectric droplets are also considered. The density, dynamic viscosity, electrical permittivity, and conductivity of *fluids 1* and *2* are $(\rho_1, \mu_1, \varepsilon_1, \sigma_1)$ and $(\rho_2, \mu_2, \varepsilon_2, \sigma_2)$, respectively. The ambient *fluid 2* is assumed to be hydrodynamically passive. The surface tension acting at the interface between *fluids 1* and *2* is

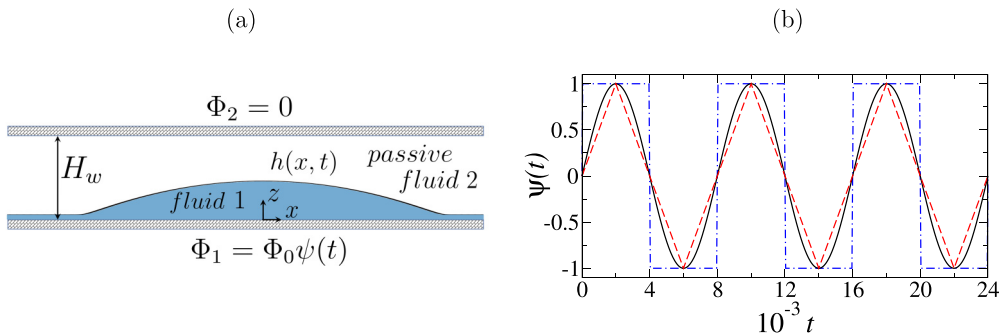


FIG. 1. (a) Schematic of a sessile droplet subjected to a periodic electrostatic forcing. The droplet is hydrodynamically active, while the ambient fluid is assumed to be hydrodynamically passive. (b) Different time-dependent waveforms of electric forcing [$\Psi(t)$] are considered in this study, namely sinusoidal (black solid line), triangular (red dashed line), and square (blue dash-dotted line).

denoted by γ . A Cartesian coordinate system (x, z) is used, where x and z represent the horizontal and vertical directions, respectively. The horizontal and vertical components of the velocity vector (\vec{v}) are denoted by u and w , respectively. The bottom wall (at $z = 0$) is held at an electric potential, $\Phi_1(0) = \Phi_0 \psi(t)$, where $\psi(t)$ represents the functional dependence of electrostatic field with time, t , and Φ_0 denotes the amplitude of the applied electric field. As an example, the electric field with a sinusoidal waveform, $\Phi_1(t) = \Phi_0 \sin(\omega t)$ implies an ac electrostatic forcing with amplitude Φ_0 and angular frequency ω . The top wall (at $z = H_w$) is grounded, i.e., $\Phi_2(H_w) = 0$. H_w is the distance between the electrodes. All parameters used in computations, unless specified otherwise, are listed in Table I. The charge relaxation time that characterizes the electrical effects are typically much larger than the magnetic timescale for most fluids encountered. Hence, the electrostatic assumption [16] is used in the present study as we take properties of such pairs of fluids for our computations. The thin-film approximation is used to obtain a reduced-order model to study the dynamics of a sessile droplet under the action of a time-dependent electric field.

A. Governing equations

The droplet (*fluid 1*) is hydrodynamically active and satisfies the continuity and the Navier-Stokes equations, which are given by

$$\nabla \cdot \vec{v}_1 = 0, \quad (1a)$$

$$\rho_1 \left(\frac{\partial \vec{v}_1}{\partial t} + \vec{v}_1 \cdot \nabla \vec{v}_1 \right) = \nabla \cdot \mathbf{T}_1 + \nabla \cdot \mathbf{M}_1 - \rho_1 g \vec{1}_z. \quad (1b)$$

Here $\mathbf{T}_1 = -p_1 \mathbf{I} + \mu_1 (\nabla \vec{v}_1 + \nabla \vec{v}_1^T)$, wherein \mathbf{I} is the identity tensor and $\vec{1}_z$ is the unit vector along positive z direction. The Maxwell stress tensor, \mathbf{M}_1 , arises due to the presence of an electric field and is given by $\mathbf{M}_1 = \varepsilon_0 \varepsilon_1 [\vec{E}_1 \vec{E}_1 - 1/2 (\vec{E}_1 \cdot \vec{E}_1) \mathbf{I}]$. Here ε_0 is the permittivity of free space, ε_1 is the

TABLE I. Physical parameters used in the numerical simulations, unless otherwise mentioned explicitly. The properties are for water-air system.

$\rho_1 = 1000 \text{ kg/m}^3$	$\varepsilon_0 = 8.854 \times 10^{-12} \text{ F/m}$
$\mu_1 = 0.9 \times 10^{-3} \text{ kg/ms}$	$\varepsilon_1 = 81, \varepsilon_2 = 1$
$H = 10^{-4} \text{ m}$	$\sigma_1 = 5.5 \times 10^{-6} \text{ S/m}, \sigma_2 = 10^{-13} \text{ S/m}$
$\gamma = 7.2 \times 10^{-2} \text{ N/m}$	$g = 9.8 \text{ m/s}^2$

permittivity of *fluid 1*, and \vec{E}_1 is the electric field in *fluid 1*. Both fluids are assumed to have no space charge in the domain and hence the electric field, $\vec{E}_i = -\nabla\Phi_i$ satisfies Gauss's law, given by

$$\nabla^2\Phi_i = 0 \quad \text{subject to } \Phi_1(0) = \Phi_0\psi(t) \quad \text{and} \quad \Phi_2(H_w) = 0. \quad (1c)$$

The above governing equation for the electric potential implies that the Maxwell stress contribution vanishes in Eq. (1b).

The interface speed (\mathcal{U}), the unit normal vector (\vec{n}) and the unit tangent vector (\vec{t}) are given by

$$\mathcal{U} = \frac{\frac{\partial h}{\partial t}}{\left[1 + \left(\frac{\partial h}{\partial x}\right)^2\right]^{1/2}}, \quad \vec{n} = \frac{-\frac{\partial h}{\partial x}\hat{i}_x + \hat{i}_z}{\left[1 + \left(\frac{\partial h}{\partial x}\right)^2\right]^{1/2}}, \quad \text{and} \quad \vec{t} = \frac{\hat{i}_x + \frac{\partial h}{\partial x}\hat{i}_z}{\left[1 + \left(\frac{\partial h}{\partial x}\right)^2\right]^{1/2}}, \quad (2)$$

respectively.

At the material fluid interface, $(\vec{v}_1 \cdot \vec{n} - \mathcal{U})$ must be equal to zero. The electric potentials are required to be continuous at the interface and together with Gauss's law yield the following conditions:

$$\Phi_1(h) = \Phi_2(h) \quad \text{and} \quad \varepsilon_0\varepsilon_1\nabla\Phi_1 \cdot \vec{n} - \varepsilon_0\varepsilon_2\nabla\Phi_2 \cdot \vec{n} = Q. \quad (3)$$

Here Q denotes the interfacial charge density. Further, the tangential and normal stress balances at the interface are given by [16]:

$$\vec{n} \cdot \mathbf{T}_1 \cdot \vec{t} = Q\vec{E} \cdot \vec{t}, \quad (4a)$$

$$\vec{n} \cdot (\mathbf{T}_1 + \mathbf{M}_1) \cdot \vec{n} - \vec{n} \cdot \mathbf{M}_2 \cdot \vec{n} = -\gamma\nabla_s \cdot \vec{n} + \frac{2s}{h_*} \left(\frac{h_*^3}{h^3} - \frac{h_*^2}{h^2} \right). \quad (4b)$$

The right-hand side of the tangential stress denotes the additional shear stress resulting due to the presence of surface charge. Here Q is the free charge density at the interface. Further, the electrostatic contribution in the normal stress balance arises due to a jump in the normal component of the Maxwell stress between the two fluids at the interface. The last term in Eq. (4b) is the conjoining-disjoining potential, with $s = \gamma(1 - \cos\theta)$ being the wetting parameter that determines the equilibrium static contact angle (θ) of the droplet [10]. The film height, h_* , corresponds to the thickness that minimizes the conjoining-disjoining potential.

The equation governing interfacial charge dynamics is obtained from charge conservation on a differential surface of the fluid interface [16]. Incorporating corrections to the surface charge density due to the motion of interface as given by Johns [28], we obtain:

$$\left[\frac{\partial Q}{\partial t} + \nabla_s \cdot (Q\vec{v}_{1s}) + Q(\nabla_s \cdot \vec{n})(\vec{v}_1 \cdot \vec{n}) \right] = \sigma_1\vec{E}_1 \cdot \vec{n} - \sigma_2\vec{E}_2 \cdot \vec{n}. \quad (5)$$

In the above, the surface velocity, $\vec{v}_{1s} = \vec{v}_1 - (\vec{v}_1 \cdot \vec{n})\vec{n}$ and the surface gradient operator, $\nabla_s = \nabla - (\vec{n} \cdot \nabla)\vec{n}$. The left-hand side is the Lagrangian rate of change of surface charge density, while the right-hand side represents the electric current density from the fluid bulk into interface. Here σ_i denotes the electrical conductivity of fluid i ($=1, 2$).

Next, we derive the thin-film model based on the separation of length scales.

B. Thin-film modelling

The following scaling based on the thin-film approximation is used to nondimensionalize the governing equations:

$$\begin{aligned} x &= \Lambda \tilde{x}, & z &= H \tilde{z}, & u &= U \tilde{u}, & w &= (\delta U) \tilde{w}, & t &= (\Lambda/U) \tilde{t}, \\ p &= (\mu_1 U/H) \tilde{p}, & \Phi_i &= \Phi_0 \tilde{\Phi}_i, & Q &= (\varepsilon_0\varepsilon_2\Phi_0/H) \tilde{Q}. \end{aligned} \quad (6)$$

The length scales in the horizontal and vertical directions are Λ and H , respectively, such that $\delta = H/\Lambda \ll 1$. Here H is the equilibrium droplet height in the absence of electric field, Λ is the

typical horizontal extent of the thin precursor film, and $\beta = H_w/H$ is the nondimensional height of the top electrode, taken to be equal to 3 for all simulations. A further restriction on the position of the top electrode is imposed such that $H_w \ll \Lambda$, and the thin-film approximation holds in the passive fluid 2 as well. The thin-film model is expected to be strictly valid only when there is a disparity of length scales, such as for the cases of highly wetting sessile droplets. However, it has been shown that the thin-film models capture the interface dynamics for sessile droplets and sessile wedges with large contact angles as well [29,30]. A heuristic estimate of the validity of the model is taken to be sessile droplets with contact angles up to 30° . We also calculated the interfacial gradient and verified that the thin-film model is valid up to a contact angle of 30° . The velocity component in the horizontal and vertical directions are scaled with a characteristic velocity scale, U and δU , respectively. The characteristic velocity scale, U , is chosen by requiring the Capillary number to be $\mathcal{O}(\delta^2)$, i.e., $U = \delta^2 \gamma / \mu$. This corresponds to the large surface tension limit, as obeyed by water or liquid metal conductors. The tildes designate dimensionless quantities. It is to be noted that the WRIBL methodology differs significantly from the conventional method of regular perturbation expansion. The problem is solved sequentially at each $\mathcal{O}(\delta)$ in a regular perturbation method. However, in the WRIBL methodology, governing equations are simply truncated to a desired $\mathcal{O}(\delta)$ accuracy. These may therefore contain terms belonging to different $\mathcal{O}(\delta)$. The field variables are then expanded in terms of appropriate basis functions and setting the weighted residues to vanish yields a mathematically consistent and converged set of evolution equations [31]. It is a well-established averaging technique for truncated governing equations based on the separation of length scales. In the current work, a WRIBL model consistent to $\mathcal{O}(\delta)$ is derived for electrowetting of a sessile droplet. The dimensionless governing equations (retaining all the terms up to $\mathcal{O}(\delta)$ and dropping the higher-order terms) are given by:

$$\frac{\partial u_1}{\partial x} + \frac{\partial w_1}{\partial z} = 0, \quad (7a)$$

$$\delta \text{Re} \left(\frac{\partial u_1}{\partial t} + u_1 \frac{\partial u_1}{\partial x} + w_1 \frac{\partial u_1}{\partial z} \right) = -\delta \frac{\partial p_1}{\partial x} + \frac{\partial^2 u_1}{\partial z^2}, \quad (7b)$$

$$-\delta \frac{\partial p_1}{\partial z} - \delta G = 0, \quad (7c)$$

where $G \equiv \rho_1 g H^2 / \mu_1 U (= \rho_1 g H^2 / \delta^2 \gamma)$ and $\text{Re} \equiv \rho_1 U H / \mu_1 (= \delta^2 \rho_1 \gamma H / \mu_1^2)$. In Eqs. (7a)–(7c), Re and G are taken to be $\mathcal{O}(1)$. No-slip and no-penetration conditions are used at the surface of the electrodes, which are given by $u_1(0) = w_1(0) = 0$. In the above and hereafter, the tilde notations have been dropped for the nondimensional variables.

In the thin-film limit, Eq. (1c) governing the potential for each phase reduces to $\frac{\partial^2 \Phi_i}{\partial z^2} = 0$, which is subject to the following boundary conditions:

$$\Phi_1(0) = \psi(t), \quad \Phi_2(\beta) = 0, \quad \Phi_1(h) = \Phi_2(h), \quad \text{and} \quad \varepsilon \frac{\partial \Phi_1}{\partial z}(h) - \frac{\partial \Phi_2}{\partial z}(h) = Q, \quad (8)$$

where the electric permittivity ratio, $\varepsilon = \varepsilon_1 / \varepsilon_2$; for the system considered here, $\varepsilon = 81$. This parameter does not appear in the perfect conductor model. Using Eq. (8), we solve for the potential in each phase as

$$\Phi_1 = \psi(t) - z \left[\frac{\psi(t) - Q(\beta - h)}{h + \varepsilon(\beta - h)} \right] \quad \text{and} \quad \Phi_2 = (\beta - z) \left[\frac{\varepsilon \psi(t) + Qh}{h + \varepsilon(\beta - h)} \right]. \quad (9)$$

The tangential and normal stress balances at the interface ($z = h$) gives:

$$\frac{\partial u_1}{\partial z} = -\delta E M^T \quad \text{and} \quad p_1 = \frac{E}{2} \left[\varepsilon \left(\frac{\partial \Phi_1}{\partial z} \right)^2 - \left(\frac{\partial \Phi_2}{\partial z} \right)^2 \right] - \frac{\partial^2 h}{\partial x^2} - S \left(\frac{h_*^3}{h^3} - \frac{h_*^2}{h^2} \right), \quad (10)$$

where $M^T = Q(\frac{\partial \Phi_1}{\partial x} + \frac{\partial \Phi_1}{\partial z} \frac{\partial h}{\partial x})$ is the tangential component of the Maxwell stress at the interface, $E \equiv \varepsilon_0 \varepsilon_2 \Phi_0^2 / \mu_1 U H (= \varepsilon_0 \varepsilon_2 \Phi_0^2 / \delta^2 \gamma H)$ is the dimensionless electric potential and $S \equiv 2s / \mu_1 U h_* (= 2s / \delta^2 \gamma h_*)$ is the dimensionless wetting parameter. Increasing the value of S signifies an increase in the static contact angle and thus decrease in the wettability of the droplet. The parameter h_* corresponds to the film thickness that minimizes the conjoining-disjoining potential and the precursor film assumes a height bounded between h_* and $1.5 h_*$ [10]. In addition, E is taken to be $\mathcal{O}(1)$. Note that the Ca is set equal to δ^2 and therefore does not appear in the normal stress balance.

Integrating the continuity equation and using the kinematic condition, we obtain $\frac{\partial h}{\partial t} = -\frac{\partial q}{\partial x}$, where the flow rate, $q = \int_0^h u_1 dz$. Integrating the vertical component of momentum balance and eliminating pressure using Eqs. (7b), (7c), and (10), we obtain

$$\delta \text{Re} \left(\frac{\partial u_1}{\partial t} + u_1 \frac{\partial u_1}{\partial x} + w_1 \frac{\partial u_1}{\partial z} \right) = -\delta E M^N + \delta \frac{\partial^3 h}{\partial x^3} + \delta S \frac{\partial}{\partial x} \left(\frac{h_*^3}{h^3} - \frac{h_*^2}{h^2} \right) - \delta G \frac{\partial h}{\partial x} + \frac{\partial^2 u_1}{\partial z^2}, \quad (11)$$

where $M^N = \frac{1}{2} \frac{\partial}{\partial x} [\varepsilon (\frac{\partial \Phi_1}{\partial z})^2 - (\frac{\partial \Phi_2}{\partial z})^2]$ is the normal component of the Maxwell stress at the interface. We now use the weighted residual technique [27] to derive the set of the reduced-order evolution equations that govern the interface position, $h(x, t)$, flow rate, $q(x, t)$, and the surface charge density, $Q(x, t)$. We first decompose the horizontal velocity component as follows:

$$u_1(x, z, t) = \underbrace{\hat{u}_1(x, z, t)}_{\mathcal{O}(1)} + \underbrace{\tilde{u}_1(x, z, t)}_{\mathcal{O}(\delta)}, \quad w_1 = -\int_0^z \frac{\partial u_1}{\partial x} dz. \quad (12)$$

Here \hat{u}_1 is an $\mathcal{O}(1)$ contribution to the velocity, while \tilde{u}_1 denotes the $\mathcal{O}(\delta)$ correction. The vertical component of velocity, w_1 [Eq. (12)] is then obtained by integrating the continuity equation. The leading-order velocity, \hat{u}_1 , is chosen to be locally parabolic at each horizontal position. This assumption is justified for moderate Reynolds numbers. Thus, \hat{u}_1 can be determined using the following equations:

$$\frac{\partial^2 \hat{u}_1}{\partial z^2} = K_u, \quad \hat{u}_1|_0 = 0, \quad \frac{\partial \hat{u}_1}{\partial z} \Big|_h = 0, \quad \int_0^h \hat{u}_1 dz = q. \quad (13)$$

Here K_u is introduced so that the leading order velocity profile is locally parabolic, and is obtained in terms of the flow rate, q using the integral constraint in Eq. (13). Next, we substitute for velocity as given by Eqs. (12) in (11) and neglect all terms of $\mathcal{O}(\delta \tilde{u}_1) = \mathcal{O}(\delta^2)$ or smaller. The only term that contains the $\mathcal{O}(\delta)$ contribution, \tilde{u}_1 , is due to viscous diffusion. This term is eliminated by taking the weighted integral of Eq. (11) with a suitable weight function. We use the Galerkin method, wherein the weight function has the same functional form as the leading order velocity, as it is the most efficient choice of weight function [27]. Thus, the weight function, F can be defined as:

$$\frac{\partial^2 F}{\partial z^2} = 1, \quad F|_0 = 0, \quad \text{and} \quad \frac{\partial F}{\partial z} \Big|_h = 0. \quad (14)$$

Using the weighted residual strategy and integrating by parts, the diffusion term gives $\int_0^h F \frac{\partial^2 u_1}{\partial z^2} dz = q + (F \frac{\partial u_1}{\partial z})|_h$. The WRIBL equation obtained from Eq. (11) is then given by

$$\begin{aligned} \int_0^h \delta \text{Re} F \left(\frac{\partial \hat{u}_1}{\partial t} + \hat{u}_1 \frac{\partial \hat{u}_1}{\partial x} + \hat{w} \frac{\partial \hat{u}_1}{\partial z} \right) dz &= q - \delta E M^T F|_h \\ &+ \left[\delta \frac{\partial^3 h}{\partial x^3} - \delta E M^N - \delta G \frac{\partial h}{\partial x} + S \frac{\partial}{\partial x} \left(\frac{h_*^3}{h^3} - \frac{h_*^2}{h^2} \right) \right] \int_0^h F dz. \end{aligned} \quad (15a)$$

Similarly, the interfacial charge equation (5) reduces to

$$\delta \left(\frac{\partial Q}{\partial t} + \hat{u}_1 \frac{\partial Q}{\partial x} + Q \frac{\partial h}{\partial x} \frac{\partial \hat{u}}{\partial z} - Q \frac{\partial \hat{w}}{\partial z} \right) = \Psi_c \left(\frac{\partial \Phi_2}{\partial z} - \sigma \frac{\partial \Phi_1}{\partial z} \right)_{z=h} \quad (15b)$$

where $\sigma = \frac{\sigma_1}{\sigma_2}$ and $\Psi_c \equiv \frac{\sigma_2 H}{\varepsilon_0 \varepsilon_2 U} (= \frac{\sigma_2 \mu_1 H}{\varepsilon_0 \varepsilon_2 \delta^2 \gamma})$. Equations (15a) and (15b) represent the thin-film WRIBL model consistent up to $\mathcal{O}(\delta)$. Substituting for velocity and F obtained from Eqs. (13) and (14), we obtain the evolution equations in terms of h , q , and Q alone. Now that the reduced order model is derived, we renormalize the system by setting $\delta = 1$ as done in Ref. [32]. This gives the final set of evolution equations as:

$$\frac{\partial h}{\partial t} + \frac{\partial q}{\partial x} = 0, \quad (16a)$$

$$\text{Re} \left(\frac{\partial q}{\partial t} + \frac{17q}{7h} \frac{\partial q}{\partial x} - \frac{9q^2}{7h^2} \frac{\partial h}{\partial x} \right) = -\frac{5q}{2h^2} - \frac{5}{4} EM^T + \frac{5h}{6} \left[\frac{\partial^3 h}{\partial x^3} - EM^N - G \frac{\partial h}{\partial x} + S \frac{\partial}{\partial x} \left(\frac{h_*^3}{h^3} - \frac{h_*^2}{h^2} \right) \right], \quad (16b)$$

$$\frac{\partial Q}{\partial t} + \frac{\partial}{\partial x} \left(\frac{3q}{2h} Q \right) = \Psi_c \left(\frac{\partial \Phi_2}{\partial z} - \sigma \frac{\partial \Phi_1}{\partial z} \right)_{z=h}, \quad (16c)$$

Equation (16) constitutes the reduced-order WRIBL model. In order to obtain Eq. (16b) from Eq. (15a), all terms were normalized to make the coefficient of $\text{Re} \frac{\partial q}{\partial t}$ unity. The terms on the left-hand side of Eq. (16b) are due to the inertial effects and are precisely the same as obtained in earlier works involving inertial WRIBL models [33,34]. The right-hand side contains terms associated with the transverse viscous diffusion, the charge-driven interfacial shear stress, the capillarity, gravity, the conjoining-disjoining potential and the normal component of the Maxwell stress. In Eq. (16c), it should be noted that the right-hand side is a function of only x and t , and independent of z . From Eq. (1c), we get

$$\frac{\partial \Phi_1}{\partial z} = - \left[\frac{\psi(t) - Q(\beta - h)}{h + \varepsilon(\beta - h)} \right] \quad \text{and} \quad \frac{\partial \Phi_2}{\partial z} = - \left[\frac{\varepsilon \psi(t) + Qh}{h + \varepsilon(\beta - h)} \right]. \quad (17)$$

It is instructive to first examine Eq. (16) for sinusoidal forcing [$\psi(t) = \sin(\omega t)$] under various limiting conditions. We initially examine the limit when both fluids are perfect dielectrics, i.e., they have negligible electrical conductivities. This limit corresponds to setting $\Psi_c \rightarrow 0$, with σ being finite in Eq. (16c). Further, as shown in Ref. [35], it is required to set the interfacial charge, Q , also to zero. Equation (16c) is then redundant and Eq. (16b) with $Q \rightarrow 0$, reduces to

$$\begin{aligned} & \text{Re} \left(\frac{\partial q}{\partial t} + \frac{17q}{7h} \frac{\partial q}{\partial x} - \frac{9q^2}{7h^2} \frac{\partial h}{\partial x} \right) \\ &= -\frac{5q}{2h^2} + \frac{5h}{6} \left\{ \frac{\partial^3 h}{\partial x^3} - G \frac{\partial h}{\partial x} + S \frac{\partial}{\partial x} \left(\frac{h_*^3}{h^3} - \frac{h_*^2}{h^2} \right) + \frac{E\varepsilon(\varepsilon - 1)^2 h [1 - \cos(2\omega t)]}{2 [\varepsilon(\beta - h) + h]^3} \frac{\partial h}{\partial x} \right\}. \end{aligned} \quad (18)$$

Here ω is the nondimensional angular frequency and is related to the nondimensional frequency, f , via the relation $2\pi f = \omega$. Equation (18) reveals that when $\varepsilon = 1$, the electrostatic term vanishes. Therefore, $\varepsilon \neq 1$ is a necessary condition for electrowetting of a pair of perfect dielectrics.

Another limit of interest is that of a perfect conducting droplet surrounded by a perfect dielectric ambient medium i.e., $\sigma \rightarrow \infty$. The equation governing interfacial charge, Eq. (16c), then simplifies to $\frac{\partial \Phi_1}{\partial z}(h) = 0$. This implies that the term within the square brackets in the definition of Φ_1 in Eq. (9) equates to zero. Thus, the potential in fluid 1 becomes independent of z and is given by $\Phi_1 = \cos(\omega t)$, with the interfacial charge given by $Q = \sin(\omega t)/(\beta - h)$. Substituting Q from Eq. (9), we

obtain $\Phi_2 = (\beta - z)/(\beta - h) \sin(\omega t)$. Equation (16b) then simplifies to:

$$\begin{aligned} & \operatorname{Re} \left(\frac{\partial q}{\partial t} + \frac{17q}{7h} \frac{\partial q}{\partial x} - \frac{9q^2}{7h^2} \frac{\partial h}{\partial x} \right) \\ &= -\frac{5q}{2h^2} + \frac{5h}{6} \left\{ \frac{\partial^3 h}{\partial x^3} - G \frac{\partial h}{\partial x} + S \frac{\partial}{\partial x} \left(\frac{h_*^3}{h^3} - \frac{h_*^2}{h^2} \right) + \frac{E [1 - \cos(2\omega t)]}{2} \frac{\partial h}{(\beta - h)^3 \partial x} \right\}. \end{aligned} \quad (19)$$

The numerical study is carried out as follows. We first determine the droplet equilibrium shape, $h_{\text{eq}}(x)$, in the absence of any electrostatic forcing. This is obtained by a transient simulation of the WRIBL model (16) with $E = Q = 0$ until a steady static droplet configuration is reached. The initial conditions ($h_{\text{in}}(x)$, $q_{\text{in}}(x)$) used to obtain the equilibrium shape are kept the same for all cases as follows:

$$q_{\text{in}}(x) = 0, \quad h_{\text{in}}(x) = \begin{cases} (1 - x^2) + h_*, & \text{if } |x| \leq 1 \\ h_*, & \text{if } |x| > 1. \end{cases} \quad (20)$$

The above initial condition ensures that the droplet volume remains constant for all equilibrium shapes obtained for different choice of parameter values such as the wetting parameter, S . The computational domain is taken to be spatially periodic to mimic the physical context of droplets arrays in digital microfluidics. These conditions are given as:

$$q(0) = q(L), \quad h(0) = h(L), \quad \frac{\partial^n h}{\partial x^n}(0) = \frac{\partial^n h}{\partial x^n}(L), \quad n = 1, 2. \quad (21)$$

We use the Fourier spectral collocation technique to obtain the numerical solutions [36]. It ensures high-order spatial resolution and the periodic spatial boundary conditions are automatically satisfied. The time integration is performed using the adaptive time-stepping *NDSolve* subroutine in Mathematica v.12.0.

Once the equilibrium droplet configuration is obtained as described above, the effect of electrostatic forcing is then investigated by solving equation (16) using the following initial conditions:

$$h(x, 0) = h_{\text{eq}}(x), \quad q(x, 0) = 0 \quad \text{and} \quad Q(x, 0) = 0, \quad (22)$$

where $h_{\text{eq}}(x)$ denotes the equilibrium shape of the drop obtained earlier in the absence of an electric field. Periodic spatial boundary conditions are imposed using the Fourier spectral collocation technique.

In Fig. 2(a), we present the temporal variations of the dimensionless droplet height, h_c , subject to a dc forcing with $E = 19.6/2$ and $S = 26.8$ using three different grid cut-off frequencies of $N = 150, 200$, and 250 . A similar result is shown for the case of ac forcing with $E = 19.6$, $f = 6.25 \times 10^{-4}$, $\operatorname{Re} = 36$, $G = 10^{-3}$, and $S = 26.8$. Comparing the results obtained using $N = 200$ and 250 reveals that the maximum relative error between them is of the order of 0.1% for dc forcing and 0.2% for ac forcing. In view of this, we have used $N = 200$ to generate the rest of the results presented in this study.

III. RESULTS AND DISCUSSION

We investigate the dynamics of the sessile droplet by varying the strength and the frequency of the ac electric field applied in the vertical direction under different limits of the leaky dielectric model with an objective to obtain a comprehensive understanding of the underlying physics. We first investigate the dynamics of a perfect conducting sessile droplet in a perfect dielectric ambient fluid ($\sigma \rightarrow \infty$). In this case, the potential everywhere within the droplet is the same as that of the bottom electrode and the dynamics of surface charge and the resulting stress at the interface is negligible. In the other limit, when the conductivity of both the droplet and the ambient fluid is very low, the model represents a perfect dielectric pair. In this case, the free charge at the interface remains identically zero. In addition to these limiting situations, we explore the parametric space for the general leaky

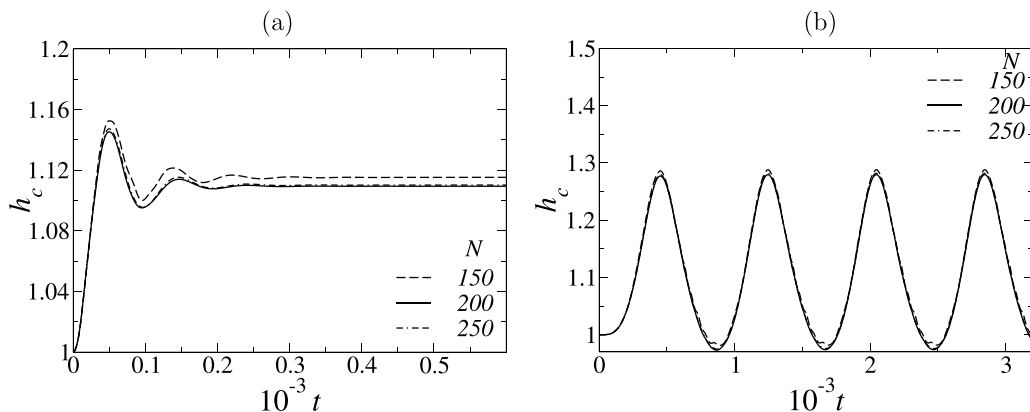


FIG. 2. The temporal variations of the dimensionless droplet height, h_c , subject to (a) dc electric forcing using different number of grid points with $E = 9.8$ and (b) ac electric forcing using different number of grid points with $E = 19.6$ and $f = 6.25 \times 10^{-4}$. The rest of the dimensionless parameters are $S = 26.8$, $G = 10^{-3}$, and $\text{Re} = 36$.

dielectric fluid to ascertain the role of various parameters on the droplet electrowetting. We consider the effect of a sinusoidal ac electric field on the above three pairs and then the effect of other time-periodic waveforms of electrostatic forcing on the sessile droplet.

A. Limit of a perfect conducting sessile droplet

We begin the presentation of our results by investigating the effect of the strength of the ac electric field, E , on a perfectly conducting sessile droplet in a perfect dielectric ambient medium. The reduced-order model corresponding to this limit consists of Eqs (16a) and (19). Figure 3 depicts the variation of the dimensionless centerline height of the droplet (h_c) with dimensionless time (t) for different values of the electrical field strength, namely $E = 19.6, 61, 100$, and 275 , with a sinusoidal frequency, $f = 6.25 \times 10^{-4}$. The value of the dimensionless wetting parameter of the droplet, S is taken to be 26.8 . It can be seen that in the presence of an ac field, h_c evolves to a periodic oscillatory state where the amplitude of the oscillation exhibit a monotonic increase

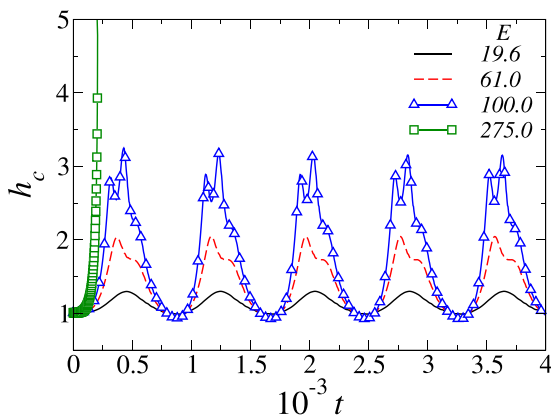


FIG. 3. The temporal variation of the dimensionless droplet height, h_c , for different values of the electric potential, E , with $f = 6.25 \times 10^{-4}$. The rest of the dimensionless parameters are $S = 26.8$, $G = 10^{-3}$, and $\text{Re} = 36$. The droplet is a perfect conductor and ambient fluid is a perfect dielectric.

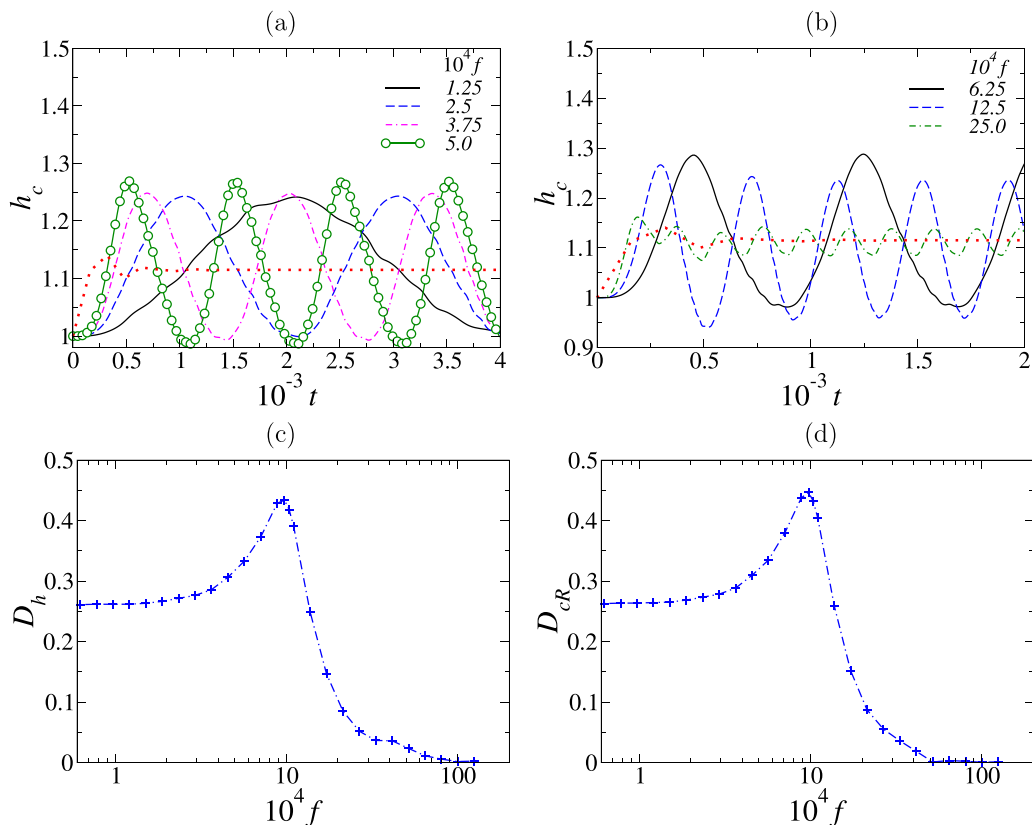


FIG. 4. [(a) and (b)] The temporal variation of the dimensionless droplet height h_c for different values of electrical field frequency: (a) the low-frequency range and (b) the high-frequency range. The variation of h_c for the equivalent dc electric field $E/2$ is shown by the red dotted line in panels (a) and (b). The variation of (c) the droplet deformation, D_h , and (d) the right contact line motion, D_{cR} , with frequency. Here a perfect conducting sessile droplet in a perfect dielectric ambient medium is considered with $E = 19.6$. The rest of the dimensionless parameters are $S = 26.8$, $G = 10^{-3}$, and $\text{Re} = 36$.

with the electrical field strength (see the results for $E \leq 100$). This trend continues until a critical field strength is reached beyond which the interface spikes upward to hit the top electrode (see the variation of h_c versus t at $E = 275$). This is analogous to the formation of a microjet in the case of a pendent droplet beyond a critical electric field strength, as reported in Ref. [20]. It can be seen that the droplet oscillates twice for each time period of electrostatic forcing. This is due to the quadratic dependence of the Maxwell stress on the electric field. As expected, the droplet deformation was found (not shown) to increase with increase in Reynolds number due to the associated decrease in viscous effects.

We now investigate the effect of the frequency of the electric field on the dynamics of droplet deformation. In Figs. 4(a) and 4(b), we have plotted the variations of the dimensionless droplet height (h_c) versus dimensionless time (t) for an applied electric field of strength, $E = 19.6$ with frequency varying in the ranges $f = 1.25 \times 10^{-4} - 5 \times 10^{-4}$ and $f = 6.25 \times 10^{-4} - 2.5 \times 10^{-3}$, respectively. The red dotted line in both panels represents the variation of h_c with t obtained under an equivalent dc field in the RMS sense, i.e., $E_{\text{dc}} = E/2$. In the dc case, it can be seen that the droplet deforms and stabilises to a steady configuration early. However, in the case of ac fields, the droplet is found to oscillate about the steady-state deformation of the equivalent dc field. Figures 4(a) and 4(b) reveal that the amplitude of the droplet oscillations increases and then decreases as the frequency

of the applied electric field is increased. This behavior is further exemplified in Fig. 4(c), which depicts the amplitude of droplet deformation, D_h , against the frequency of the applied electric field. Note that D_h is defined as the difference between the maximum and minimum values of h_c at the steady-amplitude periodic state, normalized by the steady RMS dc value of h_c . It can be observed in Fig. 4(c) that, for the parameter values considered, the amplitude of oscillations is almost constant up to $f = 2.5 \times 10^{-4}$, which then increases in the intermediate range of frequencies (1.25×10^{-4} – 9.5×10^{-4}), followed by a steep decrease with further increase in the frequency of the ac field. At very high forcing frequencies, the amplitude of the droplet oscillations saturates to zero. This is because at these high forcing frequencies, the timescale associated with the potential change is much smaller than the capillary timescale of the droplet. This makes the contact line remain almost static as if the droplet is under the influence of an equivalent dc field in the root-mean-square sense. The amplitude of contact line oscillation exhibits a similar behavior as that of the amplitude of droplet oscillation, D_h . This is evident from Fig. 4(d) which depicts the amplitude of right contact line oscillation, D_{cR} , under ac forcing as a function of the forcing frequency, f . Here D_{cR} is defined as the difference between the maximum and minimum values of the right contact line position at the steady-amplitude periodic state. It should be noted that the system is symmetric about the droplet centreline and an identical result is therefore obtained for the left contact line position. This shows that there exists an optimum forcing frequency that exhibits maximum oscillations of the droplet shape as well as the contact line motion. We next investigate whether this optimum condition exists for droplets of varying static contact angle, i.e., for different values of the wetting parameter, S .

The role of droplet wettability on droplet dynamics is investigated by considering three different values of the wetting parameter (S), viz., $S = 26.8$, $S = 14.6$, and $S = 6.8$. These values correspond to an equilibrium contact angle of 30, 22, and 15. A lower value of S corresponds to a more wetting droplet. The volume of the droplet for all values of S is kept the same. In Fig. 5(a), we have plotted droplet deformation, D_h , as a function of the forcing frequency for the three different values of S . Similarly, the effect of the wettability on the contact line motion, D_{cR} , is plotted in Fig. 5(b). A key observation can be made from Fig. 5. The less wetting droplets initially deform easily as the frequency increases due their ease in response, but at some frequency, termed the favorable frequency, a maximum in deformation is achieved. This is attributed to a competition between the characteristic time of the forcing frequency and the characteristic time of the response arising from wettability. To make this evident, we replot, in Fig. 5(c), the data presented in Fig. 5(a) by rescaling the abscissa as f/S , which is the ratio of the two characteristic times. In this graph, we see that the maximum deformation appears roughly at the same f/S for different values of S , reaffirming our reasoning.

B. Limit of a perfect dielectric drop

We now discuss the results corresponding to the limit of a perfect dielectric droplet surrounded by a perfect dielectric ambient medium. The reduced-order model corresponding to this limit consists of Eqs. (16a) and (18). The results are qualitatively similar to those observed in the case of the perfect conducting droplet as discussed in Sec. III A. In Fig. 6, the temporal variations of h_c are plotted for different values of the electrical field strengths. Similarly to Fig. 3, the amplitude of droplet oscillations exhibits a monotonic increase with the increase in the electrical field strength until the interface spikes upward for very high voltages. As in the earlier case, the interface oscillates at a frequency twice that of the forcing frequency.

The effect of the electrical field frequency on the droplet dynamics is depicted in Fig. 7(a) for lower frequencies and in Fig. 7(b) for higher frequencies. It is again clear that increasing the forcing frequency initially increases and then decreases the amplitude of the droplet oscillations. For the parameter values considered, this transition occurs at $f \sim 1 \times 10^{-3}$ as shown in Fig. 7(c). A similar trend is also observed in the contact line oscillation [Fig. 7(d)]. Therefore, like the perfect conducting droplet case, here, too, there exists an optimum forcing frequency that generates maximum oscillations in the sessile droplet.

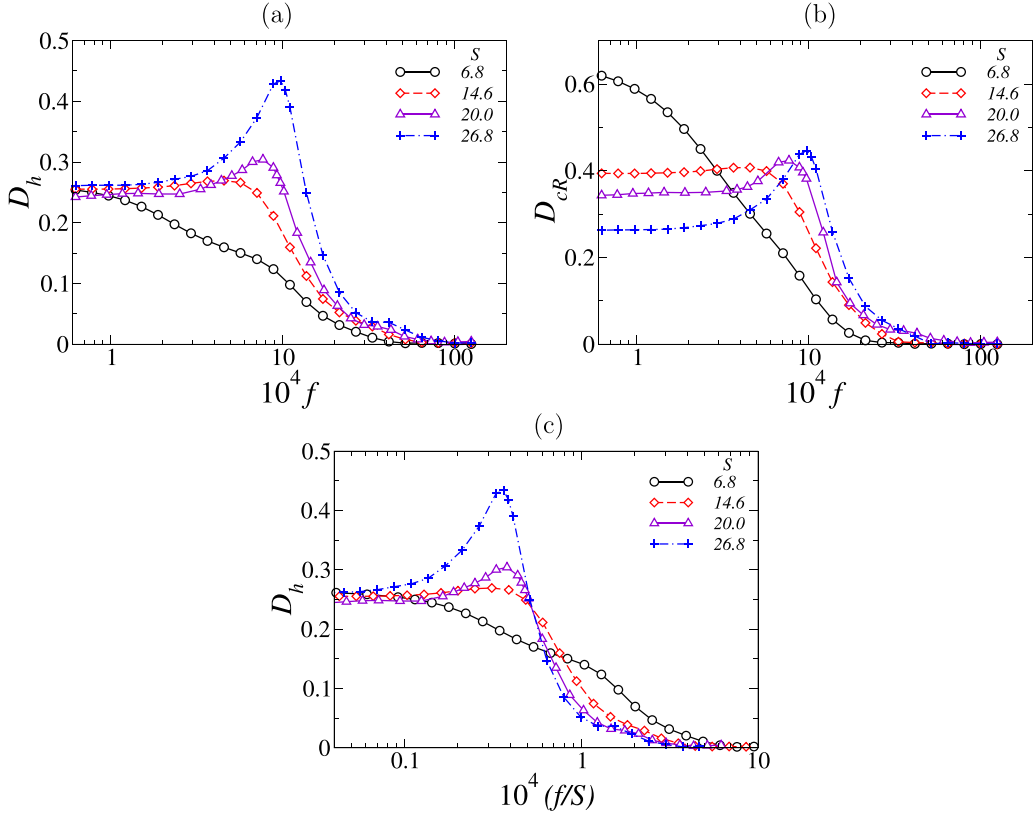


FIG. 5. The variations of (a) the deformation of the droplet, D_h and (b) the right contact line motion, D_{cR} , with frequency f for different values of the wetting parameter, S . (c) Panel (a) is replotted with the parameter, f/S , to depict the competition between forcing and wetting time scales in the problem. Here a perfect conducting sessile droplet in a perfect dielectric ambient medium is considered with $E = 19.6$. The rest of the dimensionless parameters are $G = 10^{-3}$ and $\text{Re} = 36$.

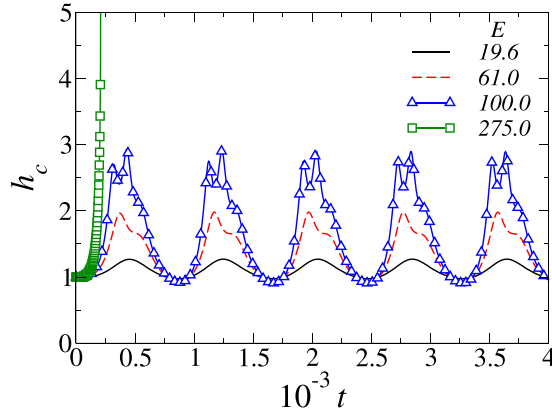


FIG. 6. The variations of the dimensionless droplet height, h_c with dimensionless time for different values of the electric potential, E , with $f = 6.25 \times 10^{-4}$, $\varepsilon = 81$. Both the droplet and ambient fluid are perfect dielectric. The rest of the dimensionless parameters are $S = 26.8$, $G = 10^{-3}$, and $\text{Re} = 36$.

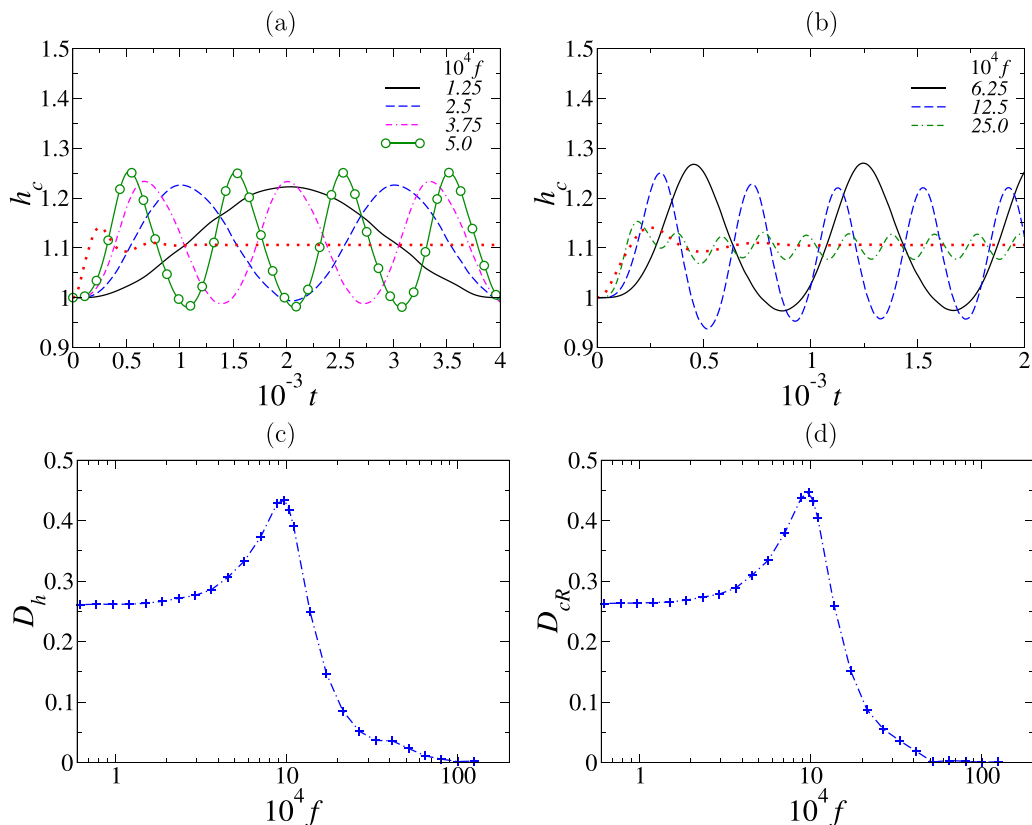


FIG. 7. [(a) and (b)] The temporal variations of the dimensionless droplet height, h_c , for different values of electrical field frequency: (a) the low-frequency range and (b) the high-frequency range. The h_c for the equivalent dc electric field is shown by the red dotted line in panels (a) and (b). The variation of (c) the droplet deformation, D_h , and (d) the right contact line motion, D_{cR} , with f . Here, a perfect dielectric sessile droplet with $S = 26.8$ in a perfect dielectric ambient medium is considered with $E = 19.6$. The rest of the dimensionless parameters are $G = 10^{-3}$ and $\text{Re} = 36$.

In Figs. 8(a) and 8(b), we present the variations of the droplet deformation, D_h , and the right contact line motion, D_{cR} , with the permittivity ratio (ε) for a perfect dielectric droplet. The parameter values considered are $E = 19.6$, $f = 6.25 \times 10^{-4}$, and $S = 26.8$. It can be seen that the amplitude of droplet oscillation as well as contact line oscillation increase with an increase in the value of permittivity ratio, ε . This is because the normal component of the Maxwell stress in the perfect dielectric system is proportional to the disparity in the permittivity between the two phases. For large values of ε , the amplitude of oscillations of the droplet is seen to saturate and the dynamics of the perfect dielectric model approaches that of the perfect conductor model. This explains why the system in Fig. 7 ($\varepsilon = 81$) gives quantitatively similar results as that of the perfect conductor model obtained in Fig. 4. Though not shown, our calculations showed a similar effect of S as in the previous case.

C. Leaky dielectric drop

Following our discussion of the extreme cases of perfect conductor–perfect dielectric pair, as well as a pair of perfect dielectrics, we now proceed to a discussion of the general leaky dielectric drop, which is the main part of the study. It was shown in Ref. [37] that a planar interface between

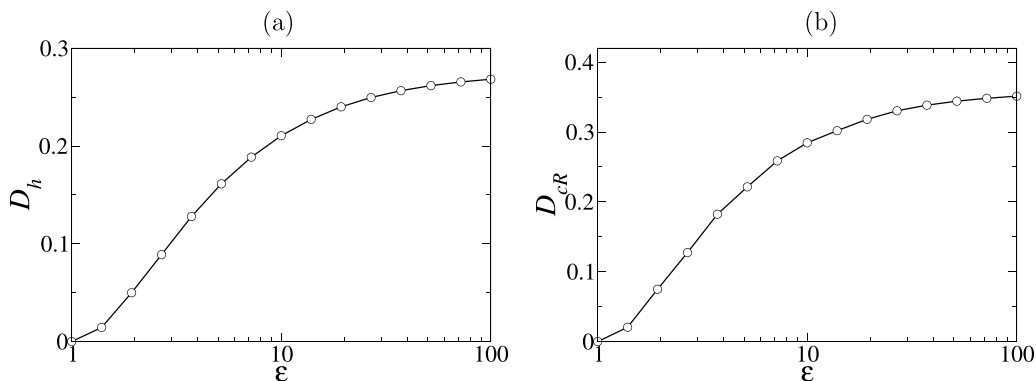


FIG. 8. The variations of (a) the droplet deformation, D_h , and (b) the right contact line motion, D_{cR} , with the permittivity ratio (ϵ) for a perfect dielectric droplet. The rest of the parameters are $E = 19.6$, $f = 6.25 \times 10^{-4}$, $G = 10^{-3}$, $Re = 36$, and $S = 26.8$.

a pair of leaky dielectric fluids undergoes markedly different dynamics depending on the electrical properties of the fluids in the ϵ - σ parameter space. In our model, we have taken the ambient fluid to be hydrodynamically passive, which typically restricts the electrical properties to the region given by $(\sigma > 1, \epsilon > 1)$. Several sets of (ϵ, σ) are chosen as shown by the markers in Fig. 9 for our numerical simulations. The point $(\epsilon, \sigma) = (1, 1)$ implies that both the droplet and the ambient fluid have identical electrical properties. In this case, no electrostatic stresses are experienced by the interface and the droplet retains its initial equilibrium shape. Along the $\sigma = \epsilon$ line, the interfacial charge remains zero and therefore charge-induced interfacial shear stress is absent. The droplet actuation is then solely due to the normal component of the Maxwell stress at the interface that arises due to a jump in electrical permittivity across the interface. As observed in earlier works on stability of planar interfaces [34,37], the interfacial charge changes its sign across the $\sigma = \epsilon$ line. Therefore the interfacial charge oscillation undergoes a complete 180° phase shift as we move across this line. This is exemplified in Fig. 10, wherein the maximum value of the interfacial charge, Q_{\max} as a function of time is plotted for five sets of parameters, namely $(\epsilon, \sigma) = (1, 4)$, $(3, 4)$, $(4, 4)$, $(5, 4)$, and $(6, 4)$, which lie on either side of the $\sigma = \epsilon$ line. The time snapshots of the droplet shape,

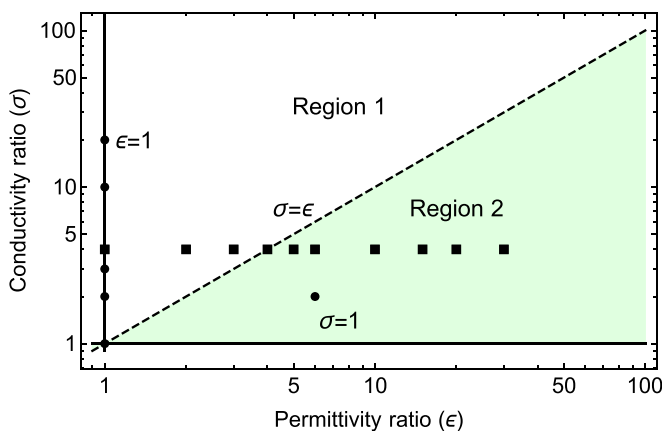


FIG. 9. Different regions in the electrical conductivity ratio (σ) and permittivity ratio (ϵ) space as shown in Ref. [37] for a planar interface between a pair of leaky dielectric fluids. The markers denote the parameter values used for nonlinear calculations.

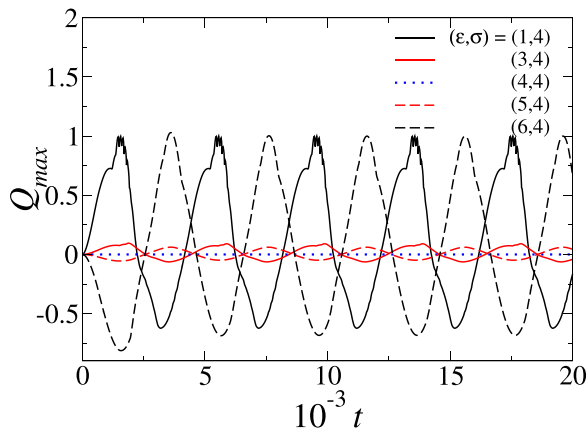


FIG. 10. Demonstration of the phase shift in the interfacial charge (Q_{\max}) oscillations as one moves across the $\sigma = \varepsilon$ curve. The droplet and the ambient medium is leaky dielectric. The rest of the parameters are $E = 4.9$, $f = 2.5 \times 10^{-4}$, $G = 10^{-3}$, $\text{Re} = 36$, and $S = 26.8$.

as well as the corresponding interface charge profile for the case of $(\varepsilon, \sigma) = (9.45, 4)$ are depicted in Figs. 11(a) and 11(b), respectively. It can be seen that there is a localized concentration of interfacial charge near the triple contact line. This surface accumulation of the charge at the triple contact line typically hinders its motion as compared to what is observed for a perfect conducting droplet, as discussed in Sec. III A. Another important observation is that though the interface shape oscillates at a frequency twice that of the forcing frequency, the interfacial charge oscillates at precisely the same frequency as the forcing frequency. This harmonicity of surface charge with the applied ac field was also noted by Oh *et al.* [15].

Next, the effect of permittivity ratio, ε is investigated by considering the response of the interface as we move toward the right along the square markers ($\sigma = 4$ line) in Fig. 9. The effect of permittivity ratio on the droplet deformation, D_h , is plotted in Fig. 12(a). It can be seen that the amplitude of droplet shape oscillation decreases, reaches a minimum and then increases with an increase in the value of permittivity ratio, ε . We see that the minimum occurs exactly at $(\varepsilon, \sigma) = (4, 4)$. This can

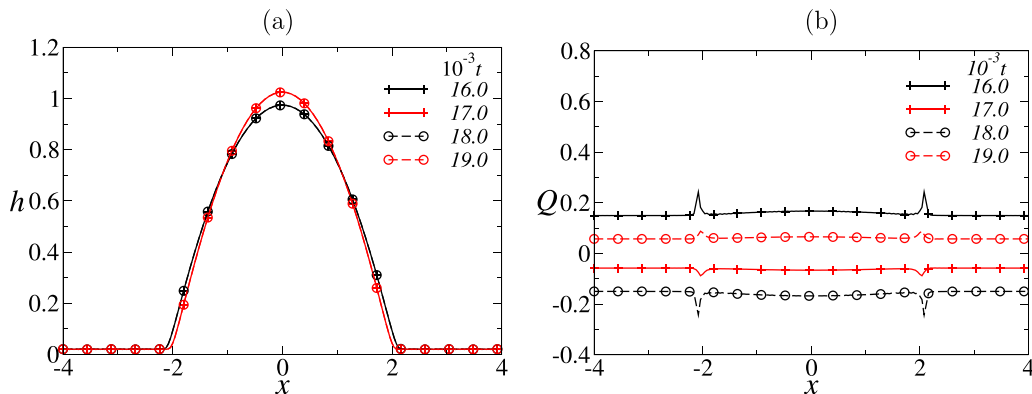


FIG. 11. (a) Time sequence of the profile of the droplet, h , and (b) the interfacial charge, Q , of a leaky dielectric droplet under a sinusoidal electrical field. The rest of the parameters are $\varepsilon = 9.45$, $\sigma = 4$, $E = 4.9$, $f = 2.5 \times 10^{-4}$, $G = 10^{-3}$, $\text{Re} = 36$, and $S = 26.8$. The image is not to scale and aspect ratio is chosen for visual clarity.

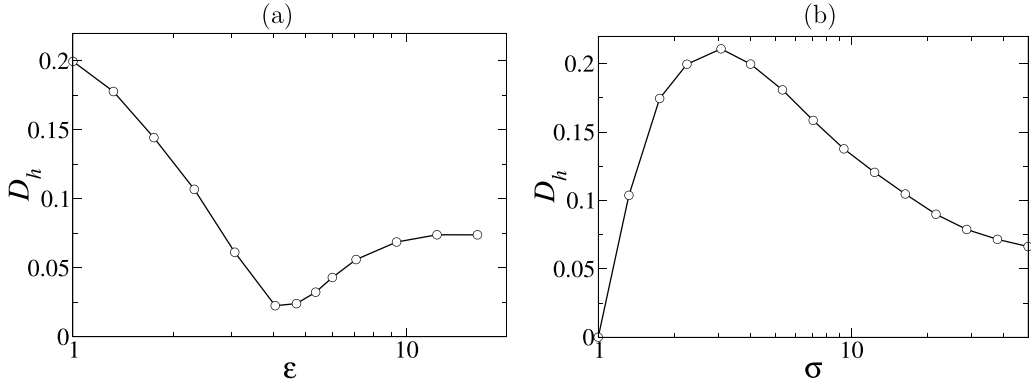


FIG. 12. (a) Effect of permittivity ratio, ϵ , on the deformation of the droplet, D_h ($\sigma = 4$) and (b) effect of conductivity ratio, σ , on the deformation of the droplet, D_h ($\epsilon = 1$) for $E = 4.9$, $f = 2.5 \times 10^{-4}$, $G = 10^{-3}$, $Re = 36$, and $S = 26.8$. The droplet and the ambient medium is leaky dielectric.

be explained based on the fact that the interface is actuated by a combined effect of the tangential and the normal component of the Maxwell stress. As we approach the $\sigma = \epsilon$ line, the role of the tangential stress is diminished, while away from the curve the increase in magnitude of the tangential stress leads to an increase in the actuation.

The effect of conductivity ratio (σ) is investigated by considering the response of the interface as we move upward along the circle markers ($\epsilon = 1$ line) in Fig. 9. The effect of conductivity ratio on the droplet deformation, D_h , is plotted in Fig. 12(b). It can be seen that with an increase in droplet conductivity, the droplet deformation initially increases, reaches a maximum and then decreases. This is explained as follows. For the case considered, i.e., $\epsilon = 1$, the Maxwell stress is dominated by its tangential component of Maxwell stress. As σ increases (departs from $\epsilon = 1$ in this case), the surface charge density increases resulting in a higher tangential Maxwell stress and an increased droplet deformation. As the conductivity ratio further increases, the system approaches a perfect conductor configuration, with uniform electric potential within the droplet. As discussed in Sec. II B, for a perfect conductor configuration, droplet deformation is possible only when a disparity exists in the permittivities of the fluid pair, i.e., $\epsilon \neq 1$. Since $\epsilon = 1$, the droplet deformation, D_h approaches zero as the system approaches the perfect conductor configuration.

Finally, in Figs. 13(a) and 13(b), we investigate the effect of other waveforms of ac electric forcing on the deformation dynamics of droplet for $E = 19.6$ and $S = 26.8$ with $f = 2.5 \times 10^{-4}$ and $f = 10.4 \times 10^{-4}$, respectively. We consider the square, the triangular and the sinusoidal waveforms of ac electric forcing and compare the temporal variation of the droplet height, h_c , obtained using these waveforms with that obtained in the case of dc electric field of equal strength. As a basis for comparison, these different waveforms were considered with equal amplitude. It should be noted here that in the case of a square waveform, the positive and the negative cycles of the electrical forcing are identical due to the quadratic dependence of the normal stress on the applied electric field. This is true for both the frequencies considered. The square wave, therefore, evokes the same response as the dc forcing. At a low frequency of $f = 2.5 \times 10^{-4}$ [cf. Fig. 13(a)], the droplet height under sinusoidal and triangular ac electric forcing attains the same peak value as that attained under the dc forcing. At a higher frequency of $f = 10.375 \times 10^{-4}$, the droplet height under sinusoidal forcing overshoots that obtained under the dc forcing. This is primarily due to inertial effects becoming dominant at higher forcing frequencies. Therefore, unlike creeping towards the steady dc height observed at low electric forcing frequencies, at higher electric frequencies, the droplet height overshoots due to the inertial oscillations. However, it is interesting to note that the amplitude of oscillations is underpredicted by a triangular waveform. Further investigation is needed to understand the behavior of droplet deformation under different waveforms.

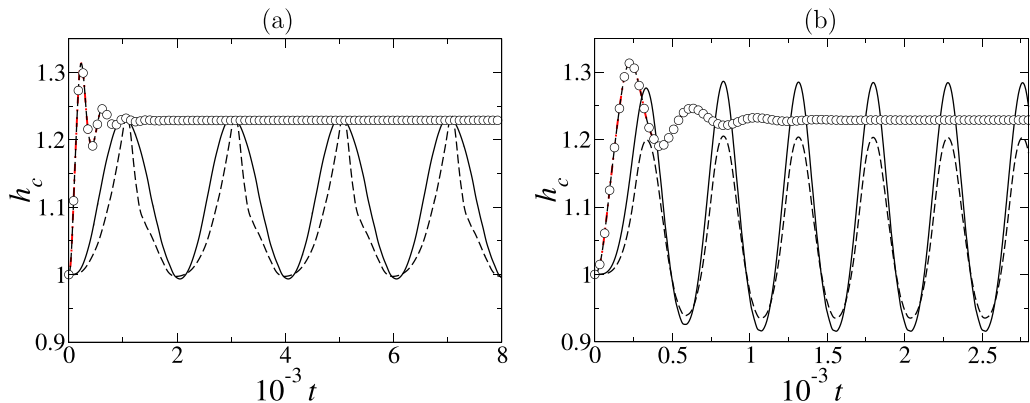


FIG. 13. Comparison of the droplet height oscillations, h_c , obtained using an ac electric forcing ($E = 19.6$) with (a) $f = 2.5 \times 10^{-4}$ and (b) $f = 8.3$ with different waveforms. The droplet is perfect conductor. The sinusoidal waveform: black solid line, the triangular waveform: dashed black line, the square waveform: red dash-dotted line and the $E = 19.6$ dc forcing: black solid line with circle symbols. The rest of the parameters are $G = 10^{-3}$, $\text{Re} = 36$, and $S = 26.8$.

IV. SUMMARY

The electrowetting and contact line dynamics of a sessile droplet in a closed coplanar configuration under time-dependent electrostatic field is investigated using a thin precursor film-based reduced-order model. The fluids are assumed to be Newtonian and leaky dielectric. The limiting cases of perfect conducting and perfect dielectric droplets have also been investigated. The dynamics observed in the case of an ac electric field is compared with an equivalent dc electric field in the root-mean-square sense. It is found that the contact line oscillates in the presence of an ac field with a frequency twice that of the forcing electric potential due to the quadratic dependence of the Maxwell stress on the applied field. The oscillation takes place about an equilibrium configuration corresponding to that of an equivalent RMS dc potential. It is found that the contact line response is monotonic with the applied strength of the electric field. An increase in the amplitude of the electric field increases the amplitude of contact line oscillations. A significant increase in the amplitude leads to spike formation and the interface ruptures at the top electrode. The contact line response can, however, become nonmonotonic with applied frequency, depending on the droplet wettability. This is a consequence of the competition between the timescale of forcing and the timescale of response as influenced by the wettability of the droplet. The parameter space of the permittivity ratio–conductivity ratio is comprehensively investigated to bring out the nontrivial role played by each of them, via their contributions to the normal and tangential components of the Maxwell stress. Different waveforms of ac forcing have also been investigated and it is shown that a square waveform acts effectively like a static dc field.

ACKNOWLEDGMENTS

D.S.P., K.C.S. and R.N. acknowledge support from SERB, India (SRG/2020/00242, CRG/2020/000507), NASA (80NSSC21K0352, NNX17AL27G), and NSF (2025117).

-
- [1] P. Paik, V. K. Pamula, M. G. Pollack, and R. B. Fair, Electrowetting-based droplet mixers for microfluidic systems, *Lab Chip* **3**, 28 (2003).
 [2] S. Wiggins and J. M. Ottino, Foundations of chaotic mixing, *Phil. Trans. R. Soc. Lond. A* **362**, 937 (2004).

- [3] F. Mugele, J.-C. Baret, and D. Steinhauser, Microfluidic mixing through electrowetting-induced droplet oscillations, *App. Phys. Lett.* **88**, 204106 (2006).
- [4] F. Mugele and J.-C. Baret, Electrowetting: From basics to applications, *J. Phys. Condens. Matter* **17**, R705 (2005).
- [5] P. G. de Gennes, Wetting: Statics and dynamics, *Rev. Mod. Phys.* **57**, 827 (1985).
- [6] G. F. Teletzke, H. T. Davis, and L. E. Scriven, How liquids spread on solids, *Chem. Eng. Comm.* **55**, 41 (1987).
- [7] D. Bonn, J. Eggers, J. Indekeu, J. Meunier, and E. Rolley, Wetting and spreading, *Rev. Mod. Phys.* **81**, 739 (2009).
- [8] D. Brutin, *Droplet Wetting and Evaporation: From Pure to Complex Fluids* (Academic Press, New York, 2015).
- [9] B. Vukasinovic, M. K. Smith, and A. Glezer, Dynamics of a sessile drop in forced vibration, *J. Fluid Mech.* **587**, 395 (2007).
- [10] J. M. Gomba and G. M. Homsy, Regimes of thermocapillary migration of droplets under partial wetting conditions, *J. Fluid Mech.* **647**, 125 (2010).
- [11] G. Karapetsas, K. C. Sahu, K. Sefiane, and O. K. Matar, Thermocapillary-driven motion of a sessile drop: Effect of non-monotonic dependence of surface tension on temperature, *Langmuir* **30**, 4310 (2014).
- [12] W. C. Nelson and C. J. Kim, Droplet actuation by electrowetting-on-dielectric (EWOD): A review, *J. Adhes. Sci. Technol.* **26**, 1747 (2012).
- [13] R. Malk, A. Rival, Y. Fouillet, and L. Davoust, EWOD in coplanar electrode configurations, in *Proceedings of ASME: ICNMM2010* (ASME, New York, NY, 2010), 232.
- [14] F. Mugele, M. Duits, and D. van den Ende, Electrowetting: A versatile tool for drop manipulation, generation and characterization, *Adv. Colloid Interface Sci.* **161**, 115 (2010).
- [15] J. M. Oh, S. H. Ko, and K. H. Kang, Shape oscillations of a drop in AC electrowetting, *Langmuir* **24**, 8379 (2008).
- [16] D. A. Saville, Electrohydrodynamics: The Taylor-Melcher leaky dielectric model, *Annu. Rev. Fluid Mech.* **29**, 27 (1997).
- [17] F. K. Wohlhuter and O. A. Basaran, Shapes and stability of pendant and sessile dielectric drops in an electric field, *J. Fluid Mech.* **235**, 481 (1992).
- [18] J. M. Oh, S. H. Ko, and K. H. Kang, Analysis of electrowetting-driven spreading of a drop in air, *Phys. Fluids* **22**, 032002 (2010).
- [19] S. R. Annapragada, S. Dash, S. V. Garimella, and J. Y. Murthy, Dynamics of droplet motion under electrowetting actuation, *Langmuir* **27**, 8198 (2011).
- [20] C. Ferrera, J. M. López-Herrera, M. A. Herrada, J. M. Montanero, and A. J. Acero, Dynamical behavior of electrified pendant drops, *Phys. Fluids* **25**, 012104 (2013).
- [21] A. Bateni, S. Laughton, H. Tavanaa, S. S. Susnar, A. Amirfazli, and A. W. Neumann, Effect of electric fields on contact angle and surface tension of drops, *J. Colloid Interface Sci.* **283**, 215 (2005).
- [22] F. Mugele, A. Staicu, R. Bakker, and D. van den Ende, Electrowetting: A versatile tool for drop manipulation, generation and characterization, *Lab Chip* **11**, 2011 (2011).
- [23] R. Malk, J. Thiesen, Y. Fouillet, and L. Davoust, EWOD-driven stirring in lab-on-a-chips: Dependence on the electrode's geometry, *Microelectron. Eng.* **97**, 306 (2012).
- [24] Y. Lu, A. Sur, C. Pascente, S. R. Annapragada, P. Ruchhoeft, and D. Liu, Dynamics of droplet motion induced by electrowetting, *Int. J. Heat Mass Transf.* **106**, 920 (2017).
- [25] H. Lee, S. Yun, S. H. Ko, and K. H. Kang, An electrohydrodynamic flow in ac electrowetting, *Biomicrofluidics* **3**, 044113 (2009).
- [26] K. C. Sahu, M. K. Tripathi, J. Chaudhari, and S. Chakraborty, Simulations of a weakly conducting droplet under the influence of an alternating electric field, *Electrophoresis* **41**, 1953 (2020).
- [27] C. Ruyer-Quil and P. Manneville, Further accuracy and convergence results on the modeling of flows down inclined planes by weighted-residual approximations, *Phys. Fluids* **14**, 170 (2002).
- [28] L. E. Johns, The diffusion equation for a solute confined to a moving surface, *Phys. Fluids* **28**, 032107 (2016).

- [29] G. Karapetsas, K. C. Sahu, and O. K. Matar, Effect of contact line dynamics on the thermocapillary motion of a droplet on an inclined plate, [Langmuir](#) **29**, 8892 (2013).
- [30] A. Wray, D. T. Papageorgiou, R. V. Craster, K. Sefiane, and O. K. Matar, Electrostatic suppression of the ‘coffee stain effect,’ [Langmuir](#) **30**, 5849 (2014).
- [31] S. Kalliadasis, C. Ruyer-Quil, B. Scheid, and M. G. Velarde, *Falling Liquid Films* (Springer, Berlin, 2012).
- [32] G. F. Dietze and C. Ruyer-Quil, Wavy liquid films in interaction with a confined laminar gas flow, [J. Fluid Mech.](#) **722**, 348 (2013).
- [33] E. Serman-Cohen, M. Bestehorn, and A. Oron, Rayleigh-Taylor instability in thin liquid films subjected to harmonic vibration, [Phys. Fluids.](#) **29**, 052105 (2017).
- [34] D. S. Pillai and R. Narayanan, Nonlinear dynamics of electrostatic Faraday instability in thin films, [J. Fluid Mech.](#) **855**, R4 (2018).
- [35] V. Shankar and A. Sharma, Instability of the interface between thin fluid films subjected to electric fields, [J. Colloid Interface Sci.](#) **274**, 294 (2004).
- [36] G. Labrosse, *Méthodes Numériques: Méthodes Spectrale: Méthodes Locales Globales, Méthodes Globales, Problèmes D’Helmoltz et de Stokes, Équations de Navier-Stokes* (Ellipses, collection Technosup, Paris, 2011).
- [37] A. K. Uguz, O. Ozen, and N. Aubry, Electric field effect on a two-fluid interface instability in channel flow for fast electric times, [Phys. Fluids.](#) **20**, 031702 (2008).